Dynamic Light Scattering and Diffusing Wave Spectroscopy Studies of the Microscopic Dynamics of Polystyrene Latex Spheres Suspended in Glycerol

by

Bradley R. Plaster

Submitted to the Department of Physics
in partial fulfillment of the requirements for the degree of

Bachelor of Science in Physics

at the

MASSACHUSETTS INSTITUTE OF TECHNOLOGY

June 1999

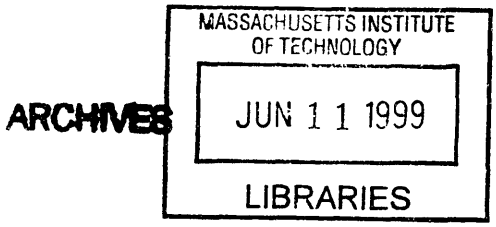

Author .....
Department of Physics
May 6, 1999

Certified by .....
Prof. Simon G. J. Mochrie
Associate Professor of Physics
Thesis Supervisor

Accepted by .....
Prof. David E. Pritchard
Senior Thesis Coordinator, Department of Physics

Dynamic Light Scattering and Diffusing Wave Spectroscopy Studies of the Microscopic Dynamics of Polystyrene Latex Spheres Suspended in Glycerol

by

Bradley R. Plaster

Submitted to the Department of Physics
on May 6, 1999, in partial fulfillment of the
requirements for the degree of
Bachelor of Science in Physics

Abstract

The dynamics of polystyrene latex spheres [650 Å radius] suspended in glycerol have been studied using the techniques of dynamic light scattering in the single scattering limit and diffusing wave spectroscopy in the multiple scattering regime using a charge coupled device [CCD] camera as our detector. Our experiments, which investigated suspensions of various concentrations [$0.001 \leq \phi \leq 0.075$], extended over length scales ranging from $q = 0.00015$ Å^{-1} to $q = 0.00071$ Å^{-1} and spanned three orders of magnitude in the time domain [0.1 s to 100 s]. Our measurements of the temporal fluctuations of the scattered intensity indicate that the dynamic behavior of our samples can be well characterized with intensity autocorrelation functions both in the single scattering limit and the multiple scattering regime.

Thesis Supervisor: Prof. Simon G. J. Mochrie
Title: Associate Professor of Physics

Acknowledgments

There are a number of people I would like to thank for their assistance with this senior thesis project. First, I would like to thank the graduate students, Peter Falus, Dirk Lumma, and Matt Borthwick, who provided me with a tremendous amount of assistance, advice, and encouragement. Peter built the apparatus which I used for my experiments and was always available to assist with any difficulties I had with the apparatus. He introduced me to the apparatus and was always eager to provide me with advice. Dirk provided me with an enormous amount of assistance with the data analysis. He was always available to assist me with the various analysis routines I used for my data analysis. Finally, Matt greatly assisted with the computer software that we used for the data analysis. He was always able to fix the numerous bugs we encountered at the onset of this project. This project would not have been possible without the constant advice and support these three were always willing to volunteer.

Last, I would like to thank my thesis supervisor, Professor Simon Mochrie, for allowing me to undertake this project. The senior thesis was definitely the most valuable component of my MIT undergraduate education and I am grateful that I was given the opportunity to work with this group.

Contents

List of Figures

Chapter 1

Introduction

Since the beginning of this century it has been known that light incident on condensed matter having local inhomogeneities in its density will scatter at angles other than the angle of incidence [1]. With the development of the laser as a source of coherent illumination at constant wavelength three decades ago, it was subsequently realized that the dynamical processes of scatterers could be monitored via measurements of the temporal intensity fluctuations of the scattered light. This general experimental technique, now known as *dynamic light scattering* (DLS), has become one of the most widely used techniques when studies of inhomogeneities on length scales of the order of the wavelength of light in physical systems are desired. The applications of DLS to various physical systems have been widespread: colloidal suspensions, gels, and polymer blends are just a few of the different physical systems that have been studied with DLS [2].

In particular, the techniques of DLS have proven to be extremely useful in investigations of colloidal suspensions of microscopic particles undergoing diffusive Brownian motion. The measurement of the temporal intensity fluctuations of the diffraction patterns of the light scattered by these particles (these diffraction patterns are known as speckle) reflects the dynamics of the scatterers. The motion of the scatterers, assumed to be random as a result of Brownian motion, subsequently results in random temporal fluctuations of the speckle intensity. These fluctuations can be characterized by an *intensity autocorrelation function* which quantifies the degree to which the

intensity fluctuations remain correlated over time. Because the intensity fluctuations are random, the fluctuations become memoryless over time, and hence the intensity autocorrelation function will decay over time [3].

Despite the fact DLS has found widespread application to the study of many different physical systems, DLS is restricted to those systems in which light is scattered at most once as a second scattering event would render measurements of the intensity autocorrelation function meaningless. Thus, prior to the development of the technique known as *diffusing-wave spectroscopy* (DWS) in 1988 [4], systems such as highly concentrated opaque colloidal suspensions which exhibit multiple scattering could not be easily studied as interpretation of the data was extremely difficult. However, under the assumption that the number of scattering events is sufficiently large such that the propagation of a photon through the scattering media becomes completely randomized, the transport of the light can be approximated as diffusive [4]. These assumptions lead to intensity autocorrelation functions which provide meaningful interpretation of temporal intensity fluctuation measurements.

This paper reports the results of both DLS and DWS experiments on samples of polystryrene latex spheres suspended in glycerol in the dilute concentration limit (the single scattering limit) and also at higher concentrations (multiple scattering) using a charge coupled device (CCD) camera as the detector. In what follows we will discuss the measurement of the intensity autocorrelation functions for these samples and the information about the dynamics of the scatterers that can be extracted from these measurements.

Chapter 2 will provide an introduction to the theory of both DLS and DWS for the specific case of a colloidal suspension in which it is assumed the particles follow a dynamical Brownian motion process. We will provide an outline of the derivations for the intensity autocorrelation functions for both DLS and DWS and an interpretation of these results.

Chapter 3 will contain a discussion of the experimental apparatus we used for our DLS and DWS experiments. We will discuss in detail the samples we investigated, the differences between the experimental set-ups we used to measure the intensity

autocorrelation functions for the DLS experiments and the DWS experiments, the CCD detector we used to measure the temporal intensity fluctuations, and the experimental method we followed in order to acquire data on these temporal intensity fluctuations.

In Chapter 4 we will continue with a description of the data analysis routine. This chapter will mainly consist of a discussion of the idea underlying the computer algorithm used to reduce the raw data to intensity autocorrelation functions.

Last, Chapter 5 will conclude with a presentation and discussion of our data on the dynamics of our samples. We will show how in the dilute concentration limit the intensity autocorrelation functions are dependent on the angle between the incident light and the detected light. For our higher concentration samples we will show how the intensity autocorrelation functions are independent of the angle between the incident light and the detected light and also how the intensity autocorrelation functions change with both variations in temperature and concentration.

Chapter 2

Theory

In this chapter we will provide an introduction to the theoretical principles underlying both DLS and DWS for the specific case of scattering from a colloidal suspension of spherical particles in solution. We assume these particles are a collection of non-interacting colloidal spheres following a dynamical Brownian motion process. Section 2.1 will develop the theory of DLS for the single scattering limit while Section 2.2 will develop the theory of DWS for the multiple scattering limit. Our discussion will largely follow those contained within [3, 5].

2.1 The single scattering limit

Let us consider a dilute sample of N colloidal particles. We will denote the position of each particle j, where $1 \leq j \leq N$, as a function of time by $\mathbf{r}_j(t)$. Laser light of constant wavelength λ illuminates the sample and each photon traversing the sample is assumed to scatter at most once. The incident wavevector, $\mathbf{k}_0$, is defined to be

$$\mathbf{k}_0 = \frac{2\pi}{\lambda}\hat{\mathbf{k}}_0, \tag{2.1}$$

where the unit vector $\hat{\mathbf{k}}_0$ defines the direction of propagation.

Light that is scattered through an angle θ will subsequently have a different wavevector, $\mathbf{k}_s$. For quasi-elastic light scattering, $|\mathbf{k}_0| = |\mathbf{k}_s|$. The scattering wavevec-

tor, $\mathbf{q}$, is then defined to be

$$\mathbf{q} \equiv \mathbf{k_s} - \mathbf{k_0}. \tag{2.2}$$

Under the assumption of quasi-elastic scattering, it is easy to show that the magnitude of $\mathbf{q}$ is

$$q = 2k_0 \sin\left(\frac{\theta}{2}\right). \tag{2.3}$$

If the magnitude of the electric field of the laser light scattered from a single particle collected at the detector is E_0, then the magnitude of the total scattered electric field, E, as a function of time at the detector can be written as the superposition of the scattered electric fields from all N particles in the sample as

$$E(t) = \sum_{j=1}^{N} E_0 e^{i\mathbf{q}\cdot\mathbf{r}_j(t)}. \tag{2.4}$$

The argument of the exponential represents the scattering phase shift that depends on the position of each particle in the sample. Because the position of each particle is a function of time, the phase of the scattered electric field from each particle also is a function of time. The magnitude of the total scattered electric field will not fluctuate over time, though. What will fluctuate over time is the scattered intensity, $I(t)$ (the physical quantity which can actually be detected), defined to be

$$I(t) = E^*(t) \cdot E(t), \tag{2.5}$$

(the * denotes the complex conjugate) which will randomly fluctuate due to the random fluctuations of the particles in the suspension.

These fluctuations can be characterized by the intensity autocorrelation function, $g_2(t)$, defined to be

$$g_2(t) \equiv 1 + \beta \frac{\langle I(t) I(t=0) \rangle}{\langle I(t=0) \rangle^2} \equiv 1 + \beta |g_1(t)|^2, \tag{2.6}$$

where β is a constant determined by the collection optics of the experimental appara-

tus, $\langle I(t)I(t=0)\rangle$ denotes the time-averaged integrated intensity, $\langle I(t=0)\rangle^2$ denotes the ensemble average of the intensity over many scattering events at $t=0$, and $g_1(t)$ is defined to be the electric field autocorrelation function. In general, $g_1(t)$ is given by

$$g_1(t) = \frac{\sum_{j=1}^{N}\sum_{k=1}^{N}\langle \exp\{i\mathbf{q}\cdot[\mathbf{r}_j(t=0)-\mathbf{r}_k(t)]\}\rangle}{\sum_{j=1}^{N}\sum_{k=1}^{N}\langle \exp\{i\mathbf{q}\cdot[\mathbf{r}_j(t=0)-\mathbf{r}_k(t=0)]\}\rangle}. \tag{2.7}$$

For the case of non-interacting (uncorrelated) particles, the cross-terms $j\neq k$ vanish to give

$$g_1(t) = \langle \exp[-i\mathbf{q}\cdot\Delta\mathbf{r}(t)]\rangle, \tag{2.8}$$

where $\Delta\mathbf{r}(t) \equiv \mathbf{r}(t) - \mathbf{r}(t=0)$. Thus, $g_1(t)$ will have decayed appreciably when $\mathbf{q}\cdot\Delta\mathbf{r}(t) \approx \pi$. If we assume the displacement of the particles, $\Delta\mathbf{r}(t)$, is a Gaussian random variable, it follows that

$$g_1(t) = \exp\left[\frac{-q^2(\Delta r(t))^2}{6}\right]. \tag{2.9}$$

A standard result of Brownian motion is that $\langle \Delta r(t)\rangle^2 = 6Dt$, where D is the particle diffusion coefficient. Thus, our final form for the intensity autocorrelation function in the single scattering limit is

$$g_2(t) = 1 + \beta\left[e^{-t/\tau}\right]^2, \tag{2.10}$$

where $\tau \equiv \frac{1}{Dq^2}$ is the time constant for the decay of g_1. Thus, in DLS measurements g_2 is expected to decay as the square of an exponential whose argument is a function of the scattering wavevector, q, and hence, the scattering angle, θ.

2.2 The multiple scattering limit and the diffusion approximation

In the multiple scattering limit, there are two different length scales which become important: the mean free path l and the transport mean free path l^*. The mean free path is defined to be the average distance between successive scattering events while the transport mean free path is defined to be the length scale over which the direction of light propagation within the sample becomes completely randomized. Because the direction of propagation is assumed to become completely randomized within the sample, the scattering wavevector, q, should have little relevance to the intensity autocorrelation function. Thus, there exist two different experimental geometries in DWS measurements: transmission and backscattering. The transmission geometry refers to the experimental geometry in which the light is incident on one side of the sample while the scattered light is collected from the other side of the sample. The backscattering geometry refers to the experimental geometry in which the light is incident on one side of the sample and the scattered light is collected from the same side of the sample. In what follows, both in our discussion of the theory and in later discussion of our experiments, we will consider only the transmission geometry.

2.2.1 The transport mean free path

As is discussed in [5], the transport mean free path will take on different values depending upon the value of k_0a, where a is the radius of the particles. If $k_0a \ll 1$, the direction of propagation will generally become randomized after a single scattering event, making $l = l^*$ in this case. For larger particles, though, several scattering events will be required before the direction of propagation becomes completely randomized, making $l^* > l$ in this case.

These two length scales can be determined experimentally by measuring the transmission coefficient T of a plane wave of light through a sample of thickness L. If $L \gg l^*$, as is usually the case, $T = \frac{3l^*}{5L}$ and almost all of the transmitted light will have been

scattered [6]. It is in this limit that the propagation of the light through the sample is assumed to be diffusive. In particular, the fundamental assumption is that each photon that propagates through the sample executes a random walk of step size l^*. In general, it is assumed that the number of steps executed will be large when $L \gg l^*$.

2.2.2 The electric field autocorrelation function for multiple scattering

The aim in this section is to sketch a derivation for the electric field autocorrelation function, g_1, as presented in [5].

In the transmission geometry, light from a laser is incident on one side of a sample of thickness $L \gg l^*$ while the scattered light is collected from the opposite side. We will assume that a single photon traversing the sample undergoes N scattering events and leaves the sample with a scattering phase that depends on its total path length, s, through the sample. The total path length is given by

$$s = \sum_{j=0}^{N} |\mathbf{r}_{j+1} - \mathbf{r}_j| = \sum_{j=0}^{N} \left(\frac{\mathbf{k}_j}{|\mathbf{k}_j|} \right) \cdot (\mathbf{r}_{j+1} - \mathbf{r}_j), \tag{2.11}$$

where $\mathbf{k}_j$ is the wavevector of the photon after j scattering events, $\mathbf{r}_j$ is the position of the jth particle that the photon scatters from, $\mathbf{r}_0$ is the position of the laser, and $\mathbf{r}_{N+1}$ is the position of the detector. Because we assume that the scattering is quasi-elastic, $k_j = k_0 \; \forall \; j$.

Thus, in analogy to the scattering phase shift we introduced in Section 2.1, the total phase shift for all N scattering events will be

$$\phi(t) = k_0 s = \sum_{j=0}^{N} \mathbf{k}_j(t) \cdot [\mathbf{r}_{j+1}(t) - \mathbf{r}_j(t)]. \tag{2.12}$$

The total scattered electric field at the detector will be a superposition of the scattered fields resulting from all possible paths through the sample. Thus, the total scattered electric field at the detector, $E(t)$, can be written as

$$E(t) = \sum_p E_p e^{i\phi_p(t)}, \tag{2.13}$$

where the sum now runs over all possible paths p, E_p is the amplitude of the scattered electric field resulting from path p, and $\phi_p(t)$ is the scattering phase shift associated with path p. This equation is of exactly the same form as Eq. (2.4). The difference is that in the single-scattering case there was only one scatterer per path, so the sum over all possible paths and all scatterers reduced to a sum only over all scatterers. Another important difference is that the scattered electric field E_p associated with a path p is no longer simply determined by the intensity of the laser beam. Instead, E_p is now dependent on both the laser beam intensity and also the number of scattering events per path.

The electric field autocorrelation function now becomes

$$g_1(t) = \frac{1}{\langle I \rangle} \left\langle \left(\sum_p E_p e^{i\phi_p(t=0)} \right) \left(\sum_{p'} E_{p'}^* e^{-i\phi_{p'}(t)} \right) \right\rangle, \tag{2.14}$$

where $\langle I \rangle$ is the total average scattered intensity at the detector. To further simplify our expression for $g_1(t)$ we will assume that terms with $p \neq p'$ in Eq. (2.14) do not contribute and the scattering phase and the electric field amplitude E_p are independent at the detector. Incorporating these assumptions gives us

$$g_1(t) = \left\langle \sum_p \frac{|E_p|^2}{\langle I \rangle} e^{i[\phi_p(t=0) - \phi_p(t)]} \right\rangle = \sum_p \frac{\langle I_p \rangle}{\langle I \rangle} \langle e^{i[\phi_p(t=0) - \phi_p(t)]} \rangle, \tag{2.15}$$

where $\langle I_p \rangle \equiv \langle |E_p|^2 \rangle$ is the average intensity from path p. We now also define

$$\begin{aligned} \Delta\phi_p(t) &= \phi_p(t) - \phi_p(t=0) \\ &= \sum_{j=0}^{N} \mathbf{k}_j(t) \cdot [\mathbf{r}_{j+1}(t) - \mathbf{r}_j(t)] - \sum_{j=0}^{N} \mathbf{k}_j(t=0) \cdot [\mathbf{r}_{j+1}(t) - \mathbf{r}_j(t=0)] \\ &= \sum_{j=1}^{N} \mathbf{q}_j \cdot \Delta\mathbf{r}_j(t) + \sum_{j=0}^{N} \Delta\mathbf{k}_j(t) \cdot [\mathbf{r}_{j+1}(t) - \mathbf{r}_j(t)], \end{aligned} \tag{2.16}$$

where we have also defined $\mathbf{q}_j \equiv \mathbf{k}_j(t=0) - \mathbf{k}_{j-1}(t=0)$, $\Delta\mathbf{k}_j(t) \equiv \mathbf{k}_j(t) - \mathbf{k}_j(t=0)$,

and $\Delta\mathbf{r}_j \equiv \mathbf{r}_j(t) - \mathbf{r}_j(t=0)$. To first-order, $\Delta\mathbf{k}_j(t) \perp [\mathbf{r}_{j+1}(t) - \mathbf{r}_j(t)]$ and therefore the second term in Eq. (2.16) can be neglected relative to the first term. Thus, Eq. (2.16) reduces to

$$\Delta\phi_p(t) = \sum_{j=1}^{N} \mathbf{q}_j \cdot \Delta\mathbf{r}_j(t). \tag{2.17}$$

where the magnitude of q is as given in Eq. (2.3).

As is discussed in greater detail in [5], under the assumption that N is very large, by the Central Limit Theorem, $\Delta\phi_p(t)$ will be a Gaussian random variable. Further, we will assume that the successive scattering phase factors, $\mathbf{q}_j \cdot \Delta\mathbf{r}_j(t)$, are independent and also that the scattering wavevectors $\mathbf{q}_j$ and the displacement vectors $\Delta\mathbf{r}_j(t)$ are independent. Under these assumptions,

$$\left\langle e^{-i\Delta\phi_p(t)} \right\rangle = e^{-\langle \Delta\phi_p^2(t) \rangle / 2}, \tag{2.18}$$

and

$$\left\langle \Delta\phi_p^2(t) \right\rangle = \frac{1}{3} N \langle q^2 \rangle \langle \Delta r^2(t) \rangle. \tag{2.19}$$

[5] discusses how the average over q^2 can be expressed in terms of the mean free path and the transport mean free path. We state the result, which is

$$\langle q^2 \rangle = 2k_0^2 \frac{l}{l^*}. \tag{2.20}$$

For long light paths (in the limit $N \gg 1$), the total path length through the sample will be $s = Nl$. Using this result and Eq. (2.20) Eq. (2.19) reduces to

$$\langle \Delta\phi_p^2(t) \rangle = \frac{2}{3} k_0^2 \langle \Delta r^2(t) \rangle \frac{s}{l^*} \tag{2.21}$$

Thus, the scattering mean free path, l, drops out of the final expression for $\langle \Delta\phi_p^2(t) \rangle$ which means the transport mean free path, l^*, is the only relevant length scale. This result implies that for length scales which are much greater than l^*, the temporal

fluctuations of the scattered light can be described within the photon diffusion approximation.

Once again using the standard Brownian motion result, $\langle \Delta r^2(t) \rangle = 6Dt$, we arrive at

$$\langle \Delta \phi_p^2(t) \rangle = 4k_0^2 Dt \frac{s}{l^*}. \tag{2.22}$$

Thus, the scattering phase shift depends only on the path length s of the light. As a result, the sum over paths in Eq. (2.13) can be rewritten as a sum over path lengths, provided that the fraction of scattered intensity associated with path p, $\frac{\langle I_p \rangle}{\langle I \rangle}$, is replaced by the fraction of the scattered intensity in paths of length s, defined to be $P(s)$.

Using all of the above results, the electric field autocorrelation function can be written as

$$g_1(t) = \sum_s P(s) \exp\left(-2k_0^2 Dt \frac{s}{l^*}\right). \tag{2.23}$$

Thus, g_1 is reduced to the problem of determining the path-length distribution of the scattered intensity, $P(s)$. By passing to the continuum limit, Eq. (2.23) becomes

$$g_1(t) = \int_0^\infty P(s) e^{-(2t/\tau)s/l^*} ds, \tag{2.24}$$

where τ, defined to be the characteristic diffusion time, is $\tau \equiv \frac{1}{k_0^2 D}$. This equation is the basis for the calculation of intensity autocorrelation functions in DWS. This result implies that a light path of length s corresponds to a random walk of $\frac{s}{l^*}$ steps which decays, on average, $e^{-2k_0^2 Dt}$, per step. The characteristic decay time for a path of length s is $\frac{\tau l^*}{2s}$ which is the time it takes for the total path length to change by $\approx \lambda$. This result indicates the most rapid decay times will come from the longest paths as the displacement of each particle will not need to be large for the entire path length to change by $\approx \lambda$.

2.2.3 The solution of the electric field autocorrelation function

The solution to Eq. (2.24) is very difficult and we will not attempt to outline the solution in detail here. The key to the solution is the determination of $P(s)$ for the experimental geometry (in our case, the transmission geometry). As is briefly discussed in [4], the method by which $P(s)$ can be calculated can be explained intuitively as follows.

It is assumed an instantaneous pulse of light is incident on some finite area of the sample at time $t = 0$. The photons that enter the sample follow a random walk process until they exit the sample. Because the time it takes each photon to traverse the sample is finite, there will be a delay between the time when the light is incident on the face of the sample and the time when it is detected after having exited the sample. This light intensity will rise to some maximum and then return to zero after all photons have exited the sample. Photons arriving at the detector a time t following the incident pulse will have traversed a distance $s = vt$ where v is the average speed of light within the sample. The flux of photons arriving at the detector will be $J_{out}(r_{out}, t)$ where r_{out} indicates the position of the detector. The flux at time t will be proportional to the fraction of photons that travel a distance $s = vt$, or, as described in the previous section, to $P(s)$. For length scales greater than the transport mean free path, the transport of light through the sample can then be modeled with the diffusion equation

$$\frac{\partial U}{\partial t} = D_l \nabla^2 U, \tag{2.25}$$

where U is the energy density of light (or alternatively, the number of photons per unit volume) and $D_l = \frac{vl^*}{3}$ is the diffusion coefficient of the light.

It is assumed that at time $t = 0$ an instantaneous pulse of light has just begun to diffuse at a distance $z_0 = \gamma l^*$ inside the sample, $\gamma > 0$. That is, because the light is randomized within the sample at a distance comparable with l^*, the incident pulse is described as an instantaneous source of diffusing light. Thus, the initial condition is

$$U(z, t = 0) = U_0\delta(z - z_0, t = 0). \tag{2.26}$$

In addition to this initial condition, the boundary condition for the diffusing light must also be specified. This is obtained by imposing the requirement that for $t > 0$ the net flux of diffusing light into the sample must be identically zero. The result is the boundary condition

$$U + \frac{2}{3}l^*\hat{\mathbf{n}}\cdot\nabla U = 0, \tag{2.27}$$

where $\hat{\mathbf{n}}$ is a normal unit vector directed out of the sample.

Using these boundary conditions, the diffusion equation, Eq. (2.25), can be solved and the resulting solution $U(\mathbf{r})$ will be valid for all points within the sample. Using this solution, the time-dependent flux of photons exiting the sample can be calculated. In addition, because all light emerging from the sample at time t has traveled a distance $s = vt$, the fraction of light, $P(s)$, that travels a distance s through the sample is simply proportional to the flux emerging at time $t = \frac{s}{v}$. Thus, $P(s)$ is given by

$$P(s) \propto |J_{out}(\mathbf{r}, t)|_{\mathbf{r}_{out}} = D_l|\hat{\mathbf{n}}\cdot\nabla U|_{\mathbf{r}_{out}}. \tag{2.28}$$

Once an expression for $P(s)$ has been obtained for a given experimental geometry, $g_1(t)$ can be calculated using Eq. (2.24).

2.2.4 The intensity autocorrelation function for the transmission geometry

The solution of $g_1(t)$ for this experimental geometry is given in [7]. For light incident from an extended plane wave source impinging on a sample of thickness L, the electric field autocorrelation function can be written as

$$g_1(t) = \frac{L}{\gamma l^*} \frac{\sinh[\gamma\sqrt{\frac{6t}{\tau}}]}{\sinh[\frac{L}{l^*}\sqrt{\frac{6t}{\tau}}]}. \tag{2.29}$$

For comparison with experiment, the intensity autocorrelation function for the transmission geometry for an extended plane wave source incident on a sample of thickness L is

$$g_2(t) = 1 + \beta \left[\frac{L}{\gamma l^*} \frac{\sinh[\gamma\sqrt{\frac{6t}{\tau}}]}{\sinh[\frac{L}{l^*}\sqrt{\frac{6t}{\tau}}]} \right]^2, \tag{2.30}$$

where again it is assumed β is a constant determined by the collection optics of the experimental geometery. The functional form appears to be complicated, but $g_2(t)$ decays nearly exponentially with time. As expected, in contrast to the single scattering limit in DLS measurements, $g_2(t)$ is independent of q and hence, the scattering angle. Thus, the collection angle of the detector should have no effect on measurements of $g_2(t)$.

Chapter 3

The experimental apparatus and procedure

In this chapter we will provide a detailed description of the experimental apparatus we used for our DLS and DWS experiments on polystryrene latex spheres suspended in glycerol and also the procedure we followed during our experiments.

3.1 The samples: polystyrene latex spheres in glycerol

The samples we chose to investigate were colloidal suspensions of polystyrene latex spheres of 650 Å radius suspended in an anhydrous glycerol solution. Glycerol was chosen because its high viscosity (approximately 14 Poise at room temperature) considerably slows the dynamics of the system thereby rendering measurements of the temporal intensity fluctuations of the speckle pattern feasible.

3.1.1 Preparation of the samples

For our experiments, we chose to investigate samples with volume fraction concentrations, which we will denote by ϕ, of 0.001, 0.005, and 0.01 in the dilute (single scattering) limit and higher volume fractions, $\phi = 0.025, 0.05,$ and 0.075, which we

expected to exhibit multiple scattering properties. To prepare these samples, we diluted pre-existing high volume fraction samples prepared at Yale University with anhydrous glycerol.

We used the following "recipe" to prepare our samples. Let α denote the volume fraction concentration of the pre-existing samples, ϕ denote the volume fraction concentration desired following dilution, M denote the mass of the pre-existing sample to be diluted, M_G denote the mass of glycerol contained within M, M_{PS} denote the mass of polystyrene contained within M, V denote the volume of the pre-existing sample to be diluted, V_G denote the volume of the glycerol contained within V, V_{PS} denote the volume of the polystyrene contained within V, ρ_G denote the density of glycerol, and ρ_{PS} denote the density of polystyrene.

It follows that

$$\alpha = \frac{V_{PS}}{V_{PS} + V_G} \text{ and } M = \rho_G V_G + \rho_{PS} V_{PS}. \tag{3.1}$$

Solving for V_{PS} and V_G gives us

$$V_{PS} = \frac{M}{\rho_{PS} + \rho_G \left(\frac{1-\phi}{\phi}\right)} \text{ and } V_G = V_{PS}\left(\frac{1-\phi}{\phi}\right). \tag{3.2}$$

Now, let G denote the mass of glycerol to be added to the pre-existing sample in order to dilute it to a ϕ volume fraction concentration. It follows that

$$\phi = \frac{V_{PS}}{V_G + V_{PS} + \frac{G}{\rho_G}} \Rightarrow G = \frac{\rho_G V_{PS}}{\phi} - \rho_G(V_{PS} + V_G). \tag{3.3}$$

The following table summarizes how our samples were prepared.

α	M (grams)	G (grams)	ϕ
0.41*	0.175	0.834	0.075
0.34*	0.267	1.689	0.05
0.26*	0.404	4.011	0.025
0.05	0.606	1.861	0.01
0.01	0.733	0.644	0.005
0.01	0.199	1.425	0.001

Table 3-1: Sample preparation

* Indicates samples prepared at Yale.

Following preparation, the samples were stored in air-tight vials until needed for measurements.

3.1.2 The sample holders

Special sample holders were constructed to hold the samples during experiments. These sample holders consisted of one stainless steel plate with a 3.7 mm deep circular hole of radius 6.4 mm and another stainless steel plate that was attached to the other plate via screws. The sample was shielded from the open air by glass windows of 1 mm thickness which were attached to the stainless steel plates with epoxy. The hole containing the sample was made air-tight with an O-ring which was placed between the two stainless steel plates. After sealing with the windows and the O-ring, the resultant thickness of the sample probed during measurements was approximately 2.2 mm thick.

3.2 The DLS experimental apparatus

3.2.1 The laser

Our source of light was a laser emitting light of constant 6328 Å wavelength manufactured by Newport. The peak power of the laser was rated at 5 milliwatts. The laser

was normally turned on at least 2 hours prior before measurements were attempted in order to ensure thermal equilibrium was established (the intensity of the laser would fluctuate to a large degree shortly after being turned on). The beam could be stopped at any time during measurements with the use of an electromechanical shutter manufactured by UniBlitz.

3.2.2 The spatial filter

The light emitted by the laser was then directed through, in the following order, a polarizer, a quarter-wave plate, and another polarizer, all of which reduced the intensity of the beam by a factor of approximately 100. The beam was then spatially filtered and then focused by a lens to a point a very short distance in front of the sample holder.

3.2.3 The sample mount

The sample holder described above was screwed onto a vertical stainless steel sample mount which was heated and cooled by a Lakeshore DRC-93C temperature controller powered by a Hewlett-Packard system power supply operated at a voltage of 12 Volts and 2 Amperes of current. In addition, to aid in maintenance of thermal equilibrium, a Endocal Refrigerated Circulating Bath filled with anti-freeze was used to circulate the anti-freeze in and out of a heat reservoir the sample mount was placed in contact with. The circulator was used to bring and subsequently maintain the temperature of the sample holder in the general vicinity of the desired temperature while the temperature controller was used to attain precise temperature levels. In addition, thermal conductivity paste was applied to the side of the sample holder in contact with the vertical sample mount prior to mounting. This temperature controlling apparatus was capable of maintaining temperatures ranging from -20 C to 80 C with a precision of ± 0.2 C.

3.2.4 The second lens and the beam stop

Upon leaving the sample, the scattered light was collected with a second lens and directed into the detector, which will be described shortly. In order to prevent the detector from becoming oversaturated due to non-scattered light near the beam center, the main beam was blocked with a beam stop (a black piece of plastic).

3.2.5 The detector

The detector we used was a Pulnix TM-7CN charge coupled device (CCD) camera capable of full frame transfer operating at room temperature. The advantage of using a CCD detector is that there exists a one-to-one mapping between the intensity of the light scattered at different scattering angles and the signal from a pixel at that scattering angle [2]. The pixel matrix of our detector was a rectangular 768×494 array with each pixel cell spanning a 8.4 μm × 9.8 μm cell. The relatively small size of each pixel results in a very high angular resolution. However, a drawback of using a CCD detector is that the primary source of noise is the dark current, and this limits the dynamic range to ~2 to 3 decades [2].

The video signal out of the camera was NTSC video format and was digitized by an 8-bit Matrox Meteor framegrabber. This framegrabber was capable of capturing and subsequently storing 640×480 pixel arrays in real time. The framegrabber was installed in a 32-bit PCI slot in a Gateway 2000 P5-166 personal computer with a 166 MHz Pentium processor, 128 megabytes of RAM, and a Linux operating system. The operation of the framegrabber was controlled with SPEC, x-ray diffraction and data acquisition software. With the operating system in place, it was possible to capture and store in memory approximately 5 data frames per second, each of which was 0.615 megabytes.

3.3 The DWS experimental apparatus

The experimental apparatus used for the DWS measurements was nearly identical to that for the DLS measurements except for three important differences. First, the lens that was previously used to collect the scattered light was eliminated. Second, the camera was focused on the glass window of the sample holder in order to detect the light immediately after having exited the sample. Third, because the camera was focused on the surface of the sample holder, the beam stop used in the DLS experimental set-up was eliminated. To block the main beam, a small piece of black electrical tape was attached to the surface of the sample holder which effectively shielded the CCD detector from oversaturation.

3.4 The experimental procedure

In this section we will describe our experimental method and the procedure which we followed to acquire our data. The samples were transferred from their air-tight vials to the sample holders with sterile plastic syringes. The sample holder was then screwed onto the sample mount after a thin coat of thermal conductivity paste was applied to the side of the sample holder in contact with the vertical sample mount. The temperature controllers were then adjusted to the desired temperature. The samples were generally allowed to sit undisturbed for approximately 30 minutes prior to the start of measurements in order to ensure that the sample had been adequately heated or cooled to the desired temperature.

As stated previously, the laser generally was turned on at least 2 hours prior to the start of measurements in order to ensure that the incident intensity would not fluctuate wildly during measurements. Also, prior to the start of measurements, all of the lights in the room were turned off in order to minimize the amount of stray light entering the CCD detector. Data was then collected as a time series of 20 dark frames (measurements made with the beam blocked by the electromechanical shutter in order to determine the level of the dark current) followed by a time series of 600

data frames (for the dilute samples) or a time series of 200 data frames (for the high volume fraction concentration samples) with each frame containing a measurement of the scattered intensity over a range of scattering angles at the time at which the frame was taken. These data sets, as described above, would then immediately be saved in real time to the hard disk with the framegrabber.

Measurements of each sample were taken at several different temperatures ranging from -10 C to 60 C. Following measurements at one temperature, the temperature controller would be reset to the desired temperature. Again, to ensure that the samples had been adequately cooled or heated prior to the start of measurements, the sample would generally be allowed to sit undisturbed for at least 30 minutes.

3.5 Calibration of the apparatus

In order to determine the scattering angle associated with each pixel, we carried out the following calibration procedure. A holographic glass plate was placed in the sample holder and mounted to the vertical sample mount. The holographic image, as imaged by the CCD camera, was a square grid partitioned into 81 small squares. The beam center was determined by averaging the coordinates of the four corners of the grid. To determine the scattering angle, the distance between the small squares, in pixels, was recorded. As the width of each of these 81 smaller squares corresponded to a scattering angle of 2 degrees, it was possible to use Eq. (2.3) in the limit of $\theta \ll 1$,

$$\begin{aligned} q &= 2k_0 \sin\left(\frac{\theta}{2}\right) \\ &= \frac{4\pi}{\lambda} \sin\left(\frac{\theta}{2}\right) \\ &\approx \frac{2\pi}{\lambda}\theta \text{ for } \theta \ll 1, \end{aligned} \tag{3.4}$$

to approximate the linear change in q per pixel, $\frac{\Delta q}{\text{pixel}}$. Knowledge of this quantity provided the basis for the one-to-one mapping between a pixel and its corresponding scattering angle.

Chapter 4

Data analysis

In this chapter we will describe the computer algorithm used to reduce the raw data (time series of 640×480 two-dimensional pixel arrays with the detected signal at each pixel corresponding to the intensity of the scattered light at the scattering angle corresponding to that particular pixel) to the desired physical quantity we intended to probe: the normalized intensity autocorrelation function. The discussion below will describe in detail the calculational procedure used to obtain an estimator for $g_2(t)$ and will largely follow that given in [8].

4.1 Preliminary definitions

As discussed in Section 2.1, the intensity autocorrelation function is defined to be

$$g_2(t) \equiv 1 + \beta \frac{\langle I(\mathbf{q},t) I(\mathbf{q},t=0) \rangle}{\langle I(\mathbf{q},t=0) \rangle^2}, \tag{4.1}$$

where we have arbitrarily defined $t = 0$ to be the time at which measurements are commenced. $I(\mathbf{q},t)$ denotes the scattered intensity (strength) at wavevector $\mathbf{q}$ at time t. We also define T to be the exposure time during which a single scattering pattern is acquired. If this exposure time, T, is smaller than the time over which the intensity autocorrelation function becomes memoryless (i.e. it decays) then the CCD pixel arrays will contain observations of what are termed speckled instances of

the scattering function. The goal of the analysis routine is to obtain an estimator for $g_2(t)$ from a series of such speckled patterns.

In what follows, the analysis routine will discuss averages over three different types of parameters. First, time-averages over sequences of data frames will be denoted by $\langle \cdots \rangle$. Second, azimuthal averages, which make use of the circular symmetry of the smoothed scattering pattern from an isotropic sample (which the samples we studied satisfy), will be denoted by $\overline{\cdots}$. Last, spatial averages over sub-regions of the pixel arrays will be denoted by $\text{avg}_R(\cdots)$, where R denotes the subregion of pixels over which the spatial average is to be calculated.

An important aspect of the analysis procedure that must be emphasized is that it is not possible to experimentally measure the instantaneous scattered intensity, $I(\mathbf{q}, t)$ due to the finite exposure time, T, of the CCD detector. However, the instantaneous scattered intensity is replaced in the analysis routine with an integral of the instantaneous scattered intensity over the exposure time. The integrated intensity, defined to be

$$\mu(\mathbf{q}, t, T) = \int_{t-\frac{T}{2}}^{t+\frac{T}{2}} I(\mathbf{q}, t)dt, \tag{4.2}$$

will replace the instantaneous scattered intensity for the remainder of this discussion. To simplify the notation, the parameter T will be excluded from our expression for the integrated intensity and will instead be referred to simply as $\mu(\mathbf{q}, t)$.

The scattered intensity as received by the CCD detector is output to the framegrabber as a time series of two dimensional pixel arrays (the data frames) which will be denoted by $I(\mathbf{s}, r)$, where $\mathbf{s} = (x, y)$, with x, y integers, denotes the pixel positions and r represents an index denoting the time steps of the data frames in the time series. It is assumed that the time steps are of approximately equidistant spacing, δt, with this spacing representing the total time necessary for the CCD detector to acquire one data frame, the framegrabber to capture and digitize this data frame, and the framegrabber to subsequently store this data frame on the hard drive of the PC. (For our experiments, δt was approximately 0.2 seconds.)

Now, the (x, y) plane of the detector is divided into pixel subregions R_i such that $R_i \cap R_j \in \emptyset \ \forall \ i \neq j$. After having found the position of the incident beam, (x_0, y_0), and the value of Δq/pixel, as described in Section 3.5, the average wavevector, $\overline{q_i}$, within some subregion R_i can be calculated by averaging over all the wavevectors, q_{i_k} in R_i, where k indexes the pixels in R_i, as

$$\overline{q_i} = \text{avg}_{R_i}\{q_{i_k}\}. \tag{4.3}$$

4.2 Partitioning reciprocal space

It is now necessary to explain the method by which reciprocal space, that is, the space spanned by the scattering wavevectors, $\mathbf{q}$, is partitioned into the subregions, R_i, described above. For all the analysis which we carried out, the R_i were concentric circles about the origin of reciprocal space (i.e. $q = 0$). The operation avg_{R_i} thus corresponds to an average in the azimuthal direction and also an average in the radial direction over some finite interval, Δq_i, of scattering wavevectors. (For the remainder of this discussion, we will discuss only the magnitude of the scattering wavevectors, q_i, and not the wavevectors, $\mathbf{q}$, themselves due to the fact our subregions R_i are concentric circles about the origin of reciprocal space.)

Several conflicting factors need to be considered when determining how to partition the reciprocal space into the above described concentric circles. Although it would be highly desirable to have an equal width Δq for each concentric ring of pixels in reciprocal space, this is in direct conflict with that fact that: 1) the scattered intensity decreases with higher wavevectors, and 2) fixed width concentric rings would lead to a decreasing number of pixels within subregions of smaller q, thereby reducing the quality of the data relative to subregions with larger values of q.

As such, an intensity-weighted algorithm was used to choose the sequence of Δq_i. This algorithm chooses a sequence Δq_i such that

$$\forall\, i,j : \sum_{q\in R_i} \langle \mu(q)\rangle^{\frac{1}{3}} = \sum_{q\in R_j} \langle \mu(q)\rangle^{\frac{1}{3}}. \tag{4.4}$$

Now, after having partitioned reciprocal space, it is then possible to obtain an estimator for the intensity autocorrelation function for each subregion of pixels, R_i. How this is accomplished is described in the next section.

4.3 The calculational procedure for estimation of $g_2(t)$

Given a time series of N two-dimensional arrays of scattered intensity speckle patterns, an estimator for $g_2(t)$ can be obtained in the following manner. The statistically unbiased estimator for the time averaged integrated intensity is $\langle \mu(q,t)\rangle \equiv \langle \mu(q)\rangle$, where

$$\langle \mu(q)\rangle = \frac{1}{N}\sum_{n=1}^{N} \mu(q,n). \tag{4.5}$$

Because parasitic scattering may exist, especially at small scattering angles, it is preferable to choose a normalization which restricts the effects of the parasitic scattering to a small number of the subregions, R_i. This is accomplished via the following normalization scheme

$$\hat{\mu}^{(i)}(q,r) = \mu(q,r)\frac{\mathrm{avg}_{R_i}\langle \mu(q)\rangle}{\mathrm{avg}_{R_i}\mu(q,r)}. \tag{4.6}$$

This normalization scheme is valid provided that $q\in R_i$.

The above construction of $\hat{\mu}^{(i)}(q,r)$ now provides the basis for a calculation of what is defined to be the temporal autocorrelation,

$$\hat{G}_2(q,k) = \frac{1}{N-k}\sum_{n=1}^{N-k} \hat{\mu}^{(i)}(q,n)\hat{\mu}^{(i)}(q,n+k), \tag{4.7}$$

where the the above expression is valid provided $q\in R_i$. (The integer k is a member of the set $\{1,\ldots,N-1\}$.) Further, subsequent normalization with the time-averaged, az-

imuthally smoothed scattered intensity pattern gives an estimator for the normalized intensity autocorrelation function,

$$g_2(q,k) = \frac{\hat{G}_2(q,k)}{\left[\overline{\langle \mu(q) \rangle}\right]^2}. \tag{4.8}$$

The relationship

$$\text{avg}_{R_i} \langle \hat{\mu}^{(i)}(q) \rangle = \text{avg}_{R_i} \langle \mu(q) \rangle, \tag{4.9}$$

justifies this choice of normalization. Finally, to obtain $g_2(q,t)$, it is simple to use the relationship $t = k\delta t$.

The choice of this estimator also allows a determination of the constant, β, in Eq. (4.1). β, known as the speckle-contrast, is the extrapolated $t = 0$ intercept of the normalized intensity autocorrelation function,

$$\lim_{t \to 0} g_2(\bar{q}_i, t) = 1 + \beta(\bar{q}_i), \tag{4.10}$$

where we have replaced q with its average magnitude, $\bar{q}_i$, in the sub-region R_i. As written, the speckle contrast as a function of the scattering wavevector, $\beta(\bar{q}_i)$, is a characteristic property reflective only of the collection optics of the experimental apparatus and independent of any sample properties.

The calculational procedure described above to obtain an estimator for $g_2(t)$ was implemented as a computer code by Dirk Lumma in the Yorick language. The intent of the code was to provide a simultaneous evaluation of $g_2(t)$ for all subregions R_i of the two-dimensional pixel array.

Chapter 5

Experimental results and discussion

The calculational procedure described in the previous chapter was used to reduce the raw data to intensity autocorrelation functions. To quantify our experimental measurements of the intensity autocorrelation functions, the data was fit using a non-linear fitting routine implemented in Yorick to the functional forms given previously in Eq. (2.10) for the low volume fraction (dilute concentration) limit and to Eq. (2.30) for the higher volume fraction concentration samples.

5.1 The single scattering limit: $\phi = 0.001, 0.005$ and 0.01

The data sets for these low volume fraction concentration samples consisted of 620 data frames (with each a two-dimensional 640×480 pixel array taken at regular time intervals of approximately 0.2 seconds), of which 20 data frames were dark frames and 600 frames were data frames.

The analysis of these data sets was performed using the code described in the previous section. The dark frames were taken in order to determine the level of the dark current, the primary source of noise in a CCD detector (as discussed in Section 3.2). To analyze the data frames, a 171×141 rectangular region of pixels was used for the analysis spanning wavevectors ranging from approximately $q = 0.000156$ Å^{-1} to

$q = 0.000376$ Å^{-1}.

To subdivide this rectangular region into the the subregions R_i described in the previous chapter, we specified that the analysis routine divide this region of reciprocal space into 18 different partitions according to the algorithm described by Eq. (4.4). The table below summarizes the number of pixels contained within each of the 18 subregions of reciprocal space.

Region	q [Å^{-1}]	Number of pixels	Region	q [Å^{-1}]	Number of pixels
1	0.000156	1181	10	0.000269	1353
2	0.000171	1222	11	0.000282	1360
3	0.000183	1202	12	0.000296	1403
4	0.000195	1233	13	0.000309	1390
5	0.000207	1283	14	0.000322	1441
6	0.000219	1277	15	0.000335	1407
7	0.000231	1329	16	0.000349	1438
8	0.000244	1334	17	0.000362	1436
9	0.000257	1371	18	0.000376	1451

Table 5-1: Partitions in reciprocal space and the number of pixels within each subregion used for analysis.

The computer code returned values for the intensity autocorrelation function $g_2(t)$. To quantify these results, a non-linear curve-fitting routine also implemented in Yorick was used to fit the returned values for $g_2(t)$ to the form for $g_2(t)$ in the single scattering limit as discussed in Section 2.1,

$$g_2(t) = 1 + \beta \left[e^{-t/\tau}\right]^2. \tag{5.1}$$

To do so, we fitted the data to the following three parameter function

$$g_2(t) = a_1 + a_2 \left[e^{-ta_3}\right]^2, \tag{5.2}$$

where the a_i denote the fitted parameters. a_1 is termed the "baseline". a_2 is the speckle-contrast discussed in Section 4.3, and $a_3 = \frac{1}{\tau}$, where, as discussed in Section 2.1, $\tau = \frac{1}{Dq^2}$.

Shown below in Figures 5-1, 5-2, and 5-3 are plots of the intensity autocorrelation functions and the fitted values of τ for the three dilute samples, $\phi = 0.001, 0.005,$ and 0.01 samples at 60 C spanning three decades of time ranging from approximately 0.1 seconds to 100 seconds.

These figures illustrate a number of the important features of the intensity autocorrelation functions we expected to observe in the single scattering limit. First, as expected in the single scattering limit, $g_2(t)$ is dependent on the scattering angle, as is evident from Figure 5.3. Second, as is also evident from Figure 5.3, in the dilute limit of single scattering, the time constants are essentially constant across concentration.

5.2 The multiple scattering limit: $\phi = 0.025, 0.05,$ and 0.075

The data sets for the samples that will be discussed in this section consisted of 220 data frames (with each a two-dimensional 640×480 pixel array taken at regular time intervals of approximately 0.2 seconds), of which 20 data frames were dark frames and 200 frames were data frames.

For these samples, we expected to observe characteristics of multiple scattering. As discussed in both [9, 10], in the multiple scattering regime, a weak localization of scattered photons around the angle of incidence in the backscattering geometry should be observed as a "cone" of scattered intensity peaked at $q = 0$ Å^{-1}. For our experiments, we did observe this same phenomenon, also termed Anderson localization (localization due to randomness) in the transmission geometry. In Figure 5-4, we show our measurements of the average correlated scattered intensity spanning a range of wavevectors ranging from approximately 2×10^{-4} Å^{-1} to 9×10^{-4} Å^{-1} for all three samples at 0 C. We were unable to observe values for the average correlated scattered intensity at lower q values because the beam stop made measurements at very low scattering angles impossible. As such, we were unable to determine the variation of

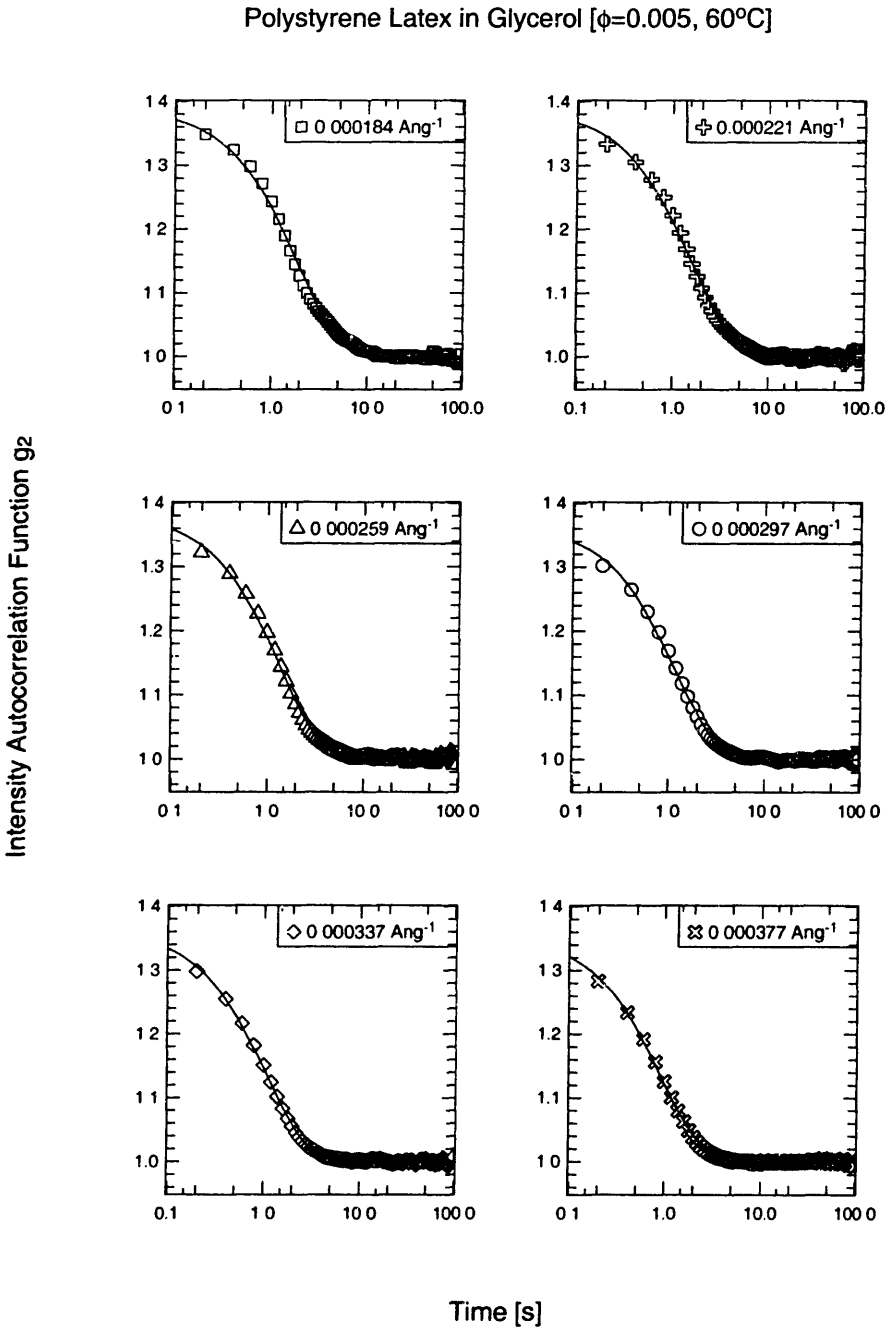

Figure 5-1: $g_2(t)$ for $\phi = 0.005$ at 60 C. Shown are 6 selected values of q. The speckle contrast is approximately constant across q with a value of $\sim$0.3 and the fitted baseline is essentially 1.

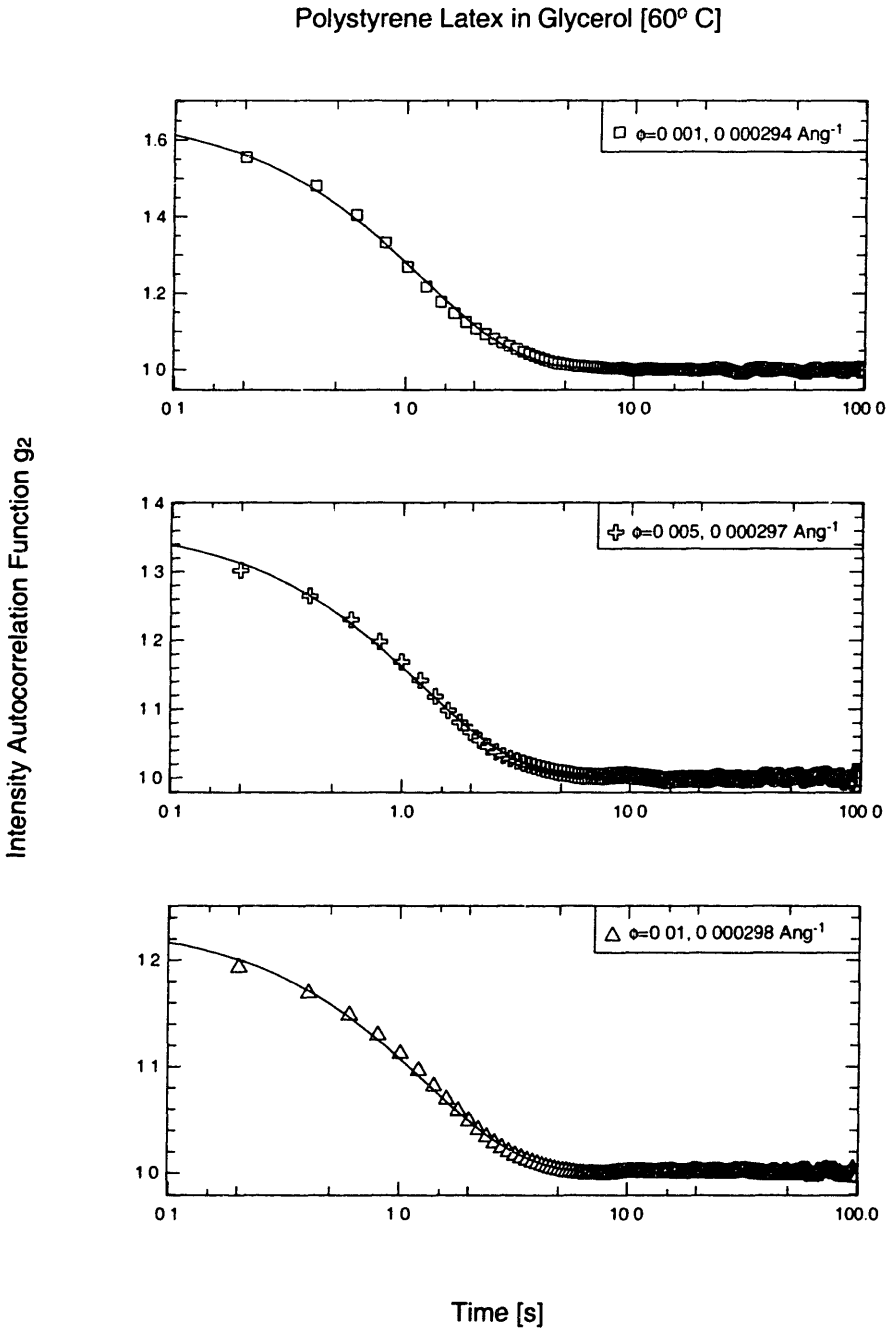

Figure 5-2: $g_2(t)$ for $\phi = 0.001, 0.005,$ and 0.01 at 60 C at approximately similar values of q. The speckle contrast varies due to the fact that the arrangement of the collection optics was slightly different for each sample. The fitted baseline, as expected, is essentially 1.

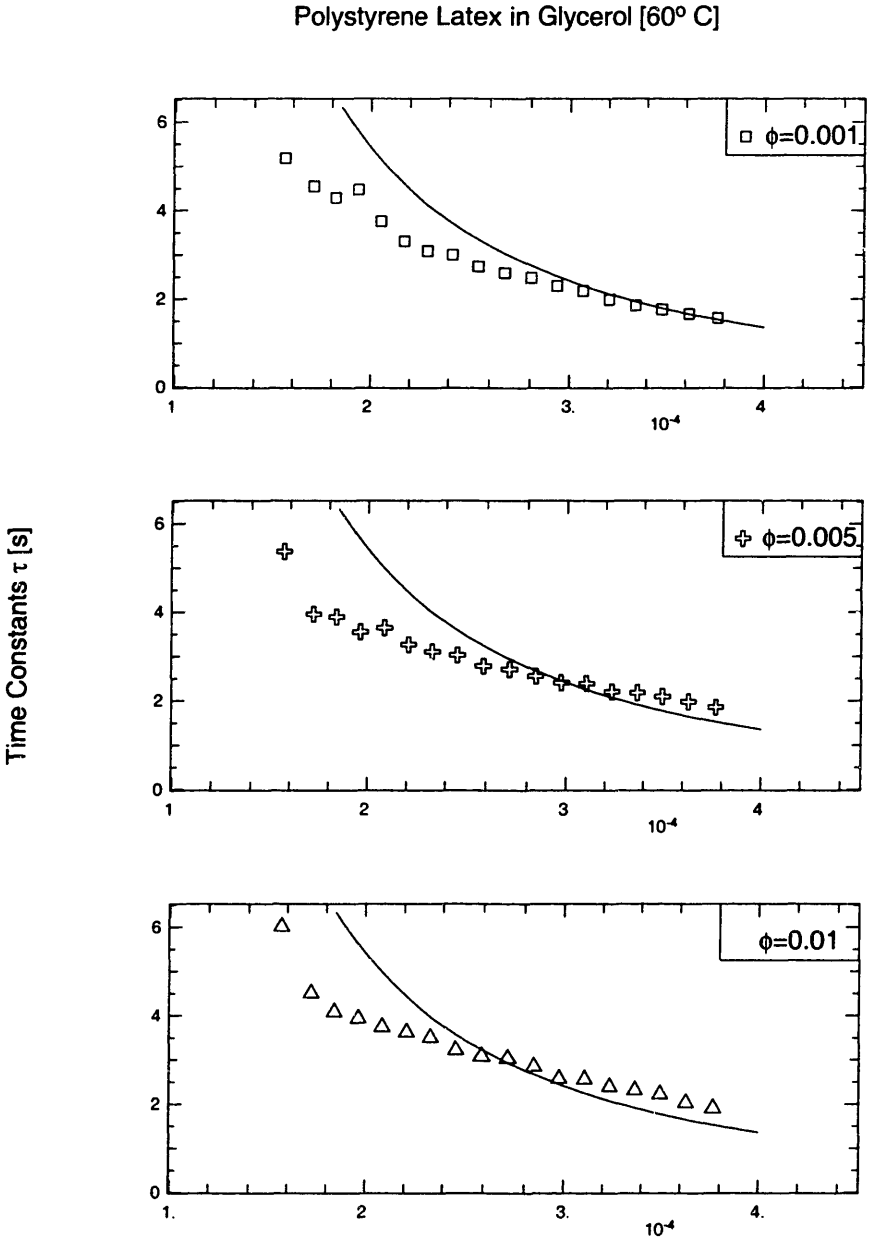

Figure 5-3: The fitted values of τ for $\phi = 0.001, 0.005$, and 0.01 at 60 C for the 18 different values of q into which reciprocal space was partitioned during the fitting routine. The solid line indicates the theoretical values we calculated for $\tau = \frac{1}{Dq^2}$. We note our fitted values do not correspond precisely with the theoretical values which we attribute to experimental error.

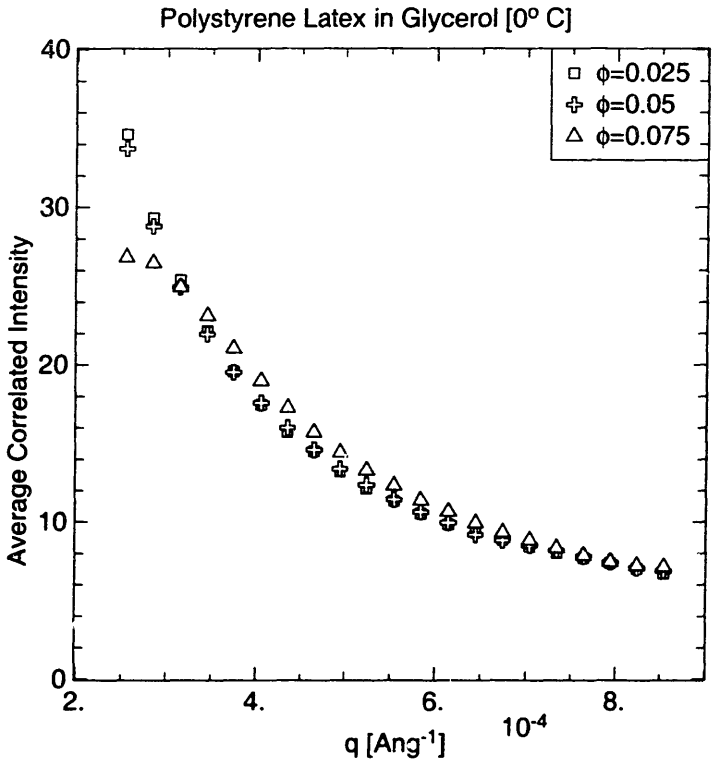

Figure 5-4: The average correlated scattered intensity for $\phi = 0.025, 0.05$, and 0.075 at 0 C.

the cone's height at $q = 0$ Å^{-1} over concentration.

The variations in the magnitude of the scattered intensity appear to be fairly constant across concentration. However, the scattered intensity does appear to increase slightly with concentration, as expected. As previously stated, a better verification would have been obtained if we had been able to observe the value of the scattered intensity at $q = 0$ Å^{-1}, as both [9, 10] report that the height of the cone should increase with concentration.

To perform the analysis of these data sets, we again used the code described in Chapter 4. Again, 20 dark frames were taken in order to determine the level of the noise (the dark current) followed by a time series of 200 data frames. To analyze these data frames, a 201×201 square region of pixels centered at $q = 0$ Å^{-1} spanning wavevectors ranging from approximately $q = 0.000158$ Å^{-1} to $q = 0.000714$ Å^{-1} was used for the analysis.

To divide this region into the R_i subregions discussed in Chapter 4, we specified

that the analysis divide this region of reciprocal space into 9 different partitions according to the algorithm described by Eq. (4.4). The following table summarizes the number of pixels contained within each of these 9 subregions of reciprocal space.

Region	q [Å^{-1}]	Number of pixels
1	0.000158	4896
2	0.000274	3436
3	0.000342	3808
4	0.000403	4140
5	0.000460	4416
6	0.000513	4640
7	0.000563	4836
8	0.000615	4944
9	0.000714	5276

Table 5-2: Partitions in reciprocal space and the number of pixels within each subregion used for analysis.

The computer code again returned values for the intensity autocorrelation function, $g_2(t)$. To quantify our results, the same non-linear fitting routine written in Yorick used in the single scattering limit was used to fit the returned values of $g_2(t)$ to the form for $g_2(t)$ in the multiple scattering limit as discussed in Section 2.2.4,

$$g_2(t) = 1 + \beta \left[\frac{L}{\gamma l^*} \frac{\sinh[\gamma\sqrt{\frac{6t}{\tau}}]}{\sinh[\frac{L}{l^*}\sqrt{\frac{6t}{\tau}}]} \right]^2 . \tag{5.3}$$

If the non-linear curve fitting routine were used for this function, the fit would a require five parameter function,

$$g_2(t) = a_1 + a_2 \left[\frac{a_3}{a_4} \frac{\sinh[a_4\sqrt{6ta_5}]}{\sinh[a_3\sqrt{6ta_5}]} \right]^2 , \tag{5.4}$$

where the a_i denote the fitted parameters. [a_1 is again the baseline, a_2 is the speckle-contrast, $a_3 = \frac{L}{l^*}$, $a_4 = \gamma$, and $a_5 = \frac{1}{\tau} = Dk_0^2$.]

However, using a five-parameter fit would make the fitting results fairly inaccurate. Thus, our goal was to reduce the above five-parameter fit to a three-parameter fit via experimental measurement of the ratio $\frac{L}{l^*}$ and calculation of the characteristic diffusion time, τ.

To experimentally measure $\frac{L}{l^*}$, as discussed in Section 2.2.1, we measured the transmitted power for the three samples and compared this to the transmitted power for a sample cell containing only anhydrous glycerol. Our results are summarized in the following table. The $\phi = 0$ sample refers to the sample cell containing only glycerol and the units of power are in microwatts.

ϕ	Power [μW]	$\frac{L}{l^*}$
0	62.0	—
0.025	5.44	6.84
0.05	1.91	19.48
0.075	1.23	30.24

Table 5-3: Transmitted intensity measurements and the experimental determination of $\frac{L}{l^*}$.

A graph of our values for $\frac{L}{l^*}$ as a function of concentration are plotted in Figure 5-5. As expected for volume fractions less than approximately 0.1, the data points are nearly linear [6]. A linear regression of these three data points in which we forced the intercept to be zero gave us

$$\frac{L}{l^*} = (390.1 \pm 93)\phi. \tag{5.5}$$

To calculate values for the characteristic diffusion time, $\tau = \frac{1}{Dk_0^2}$, we assumed that $D = D_0$, where D_0 is the Einstein-Stokes diffusion coefficient, defined to be

$$D_0 = \frac{k_B T}{6\pi\eta a}, \tag{5.6}$$

where k_B is Boltzmann's constant, T is the temperature as measured in Kelvins, η is the viscosity of anhydrous glycerol, and a is the radius of the particles. Using the

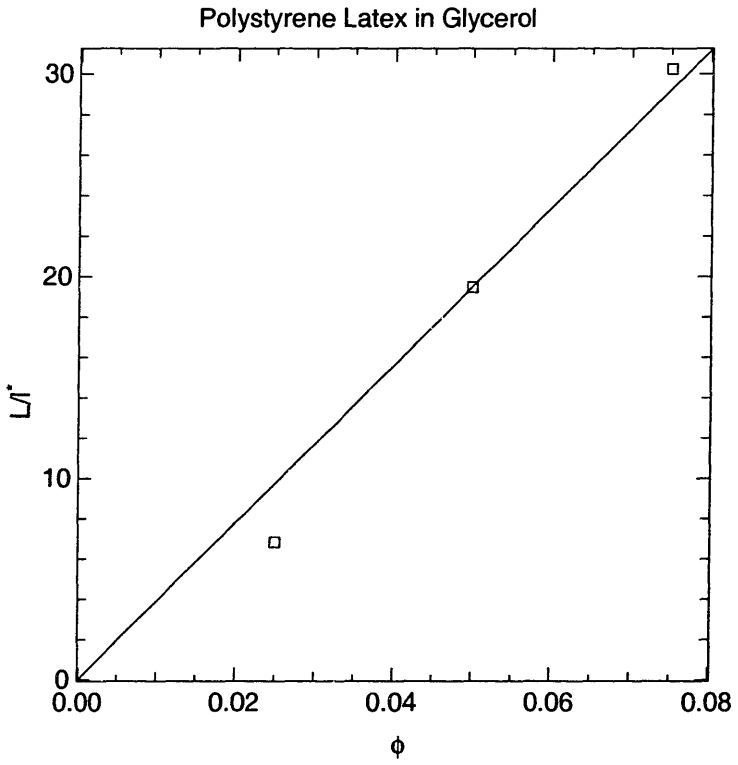

Figure 5-5: Experimentally measured values of $\frac{L}{l^*}$ for $\phi = 0.025, 0.05$ and 0.075.

calculated values for D_0 and the wavevector of the incident light, $k_0 = 0.000993$ Å^{-1}, we were able to calculate the following values for τ as summarized within the following table. (Note: we assumed that the value of D_0 at constant temperature was constant for all three samples.) The temperature values are given in degrees Celcius.

T	τ
-10	119.8
0	39.8
10	12.4

Table 5-4: Calculation of $\tau = \frac{1}{Dk_0^2}$ for -10 C, 0 C and 10 C.

With our measured values of $\frac{L}{l^*}$ and our calculated values for τ, the five-parameter fit was reduced to the following three-parameter fit

$$g_2(t) = a_1 + a_2 \left[\frac{L/l^*}{a_3} \frac{\sinh[a_3\sqrt{\frac{6t}{\tau}}]}{\sinh[\frac{L}{l^*}\sqrt{\frac{6t}{\tau}}]} \right]^2, \tag{5.7}$$

where a_1 is the fitted baseline, a_2 is the speckle-contrast, and $a_3 = \gamma$.

Shown below in Figures 5-6, 5-7, and 5-8 are plots of the intensity autocorrelation functions and their fits for the three samples, $\phi = 0.025, 0.05,$ and 0.075. The fits were performed holding the values for $\frac{L}{l^*}$ and τ constant at the values determined above. For our data, the fitted values of γ ranged from approximately 2 to 20, consistent with the values of γ given in [4]. We show these in Figure 5-9. The figures provide a basis for comparison across wavevector ranges, temperature, and concentration. All of our data spans two decades of time, ranging from approximately 0.1 seconds to 10 seconds.

These figures illustrate a number of the important features of the intensity autocorrelation functions we expected to observe in the multiple scattering limit. First, as shown in Figure 5-6, $g_2(t)$ appears to be independent of the scattering angle. Second, as shown in Figure 5-7, the data is fit well using our calculated values for τ, which decrease with increasing temperature. This reflects the fact that the dynamics of these samples "speed up" with increasing temperature, reflecting the expected scaling of the diffusion coefficient, D_0, with temperature. Third, as shown in Figure 5-8, our measurements indicate that the intensity autocorrelation functions decay faster with increasing concentration for the range of volume fractions we investigated.

5.3 Conclusion

We have performed a study of the dynamics of polystyrene latex spheres in glycerol using the light-scattering techniques of dynamic light scattering and diffusing-wave spectroscopy employing a charge coupled device (CCD) camera as our detector. We probed the dynamics of our samples via temporal measurements of the scattered intensity across a range of scattering angles which we quantified with intensity autocorrelation functions. Our measurements explored the dynamics of three dilute samples in the single scattering limit, with volume fractions $\phi = 0.001, 0.005,$ and 0.01, and three samples which we expected to exhibit multiple scattering properties, $\phi = 0.025, 0.05,$ and 0.075. Our measurements in the single scattering limit spanned

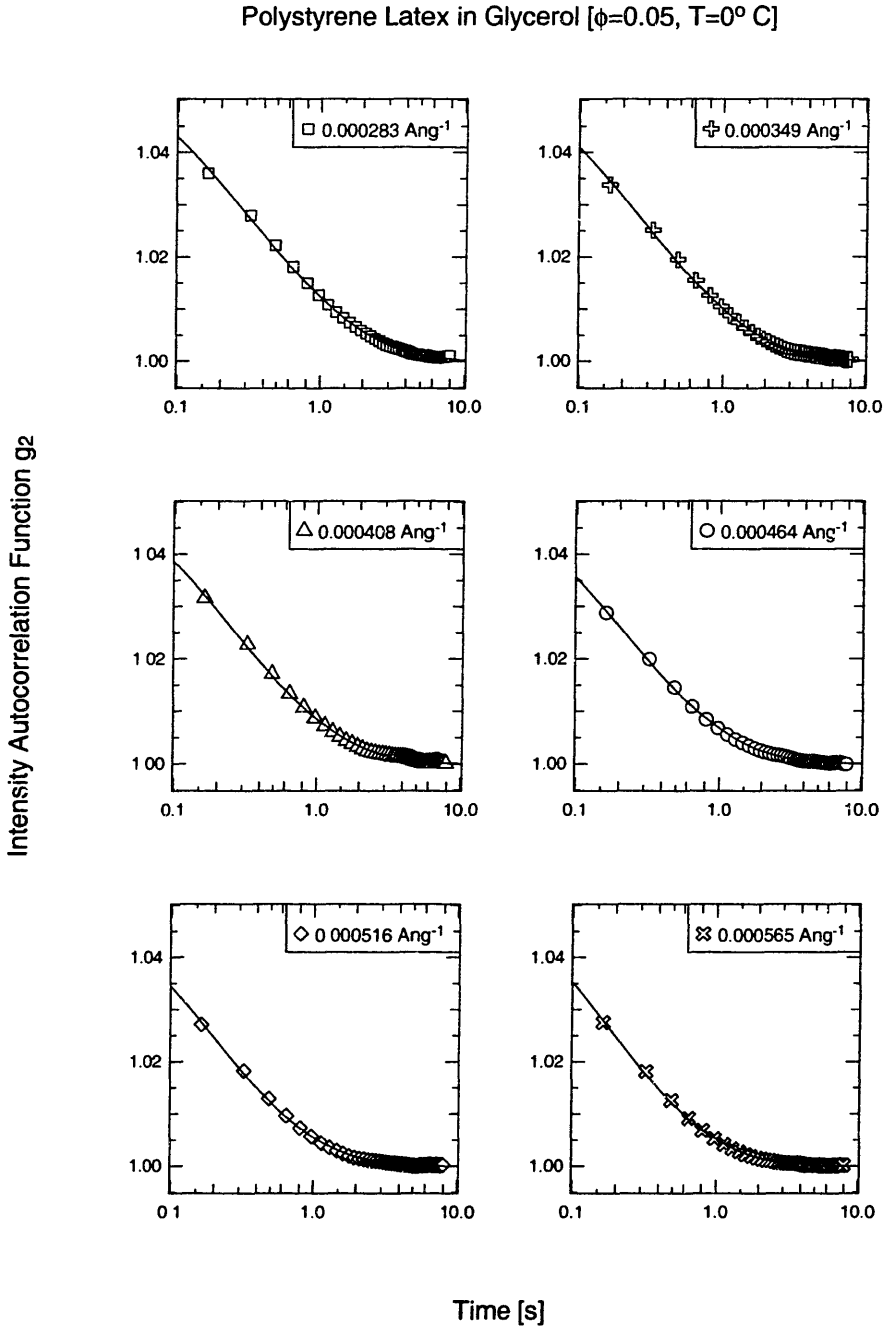

Figure 5-6: $g_2(t)$ for $\phi = 0.05$ at 0 C. Shown are 6 selected values of q. The speckle contrast is nearly constant across q with a value of $\sim$0.04 and the fitted baseline is essentially 1.

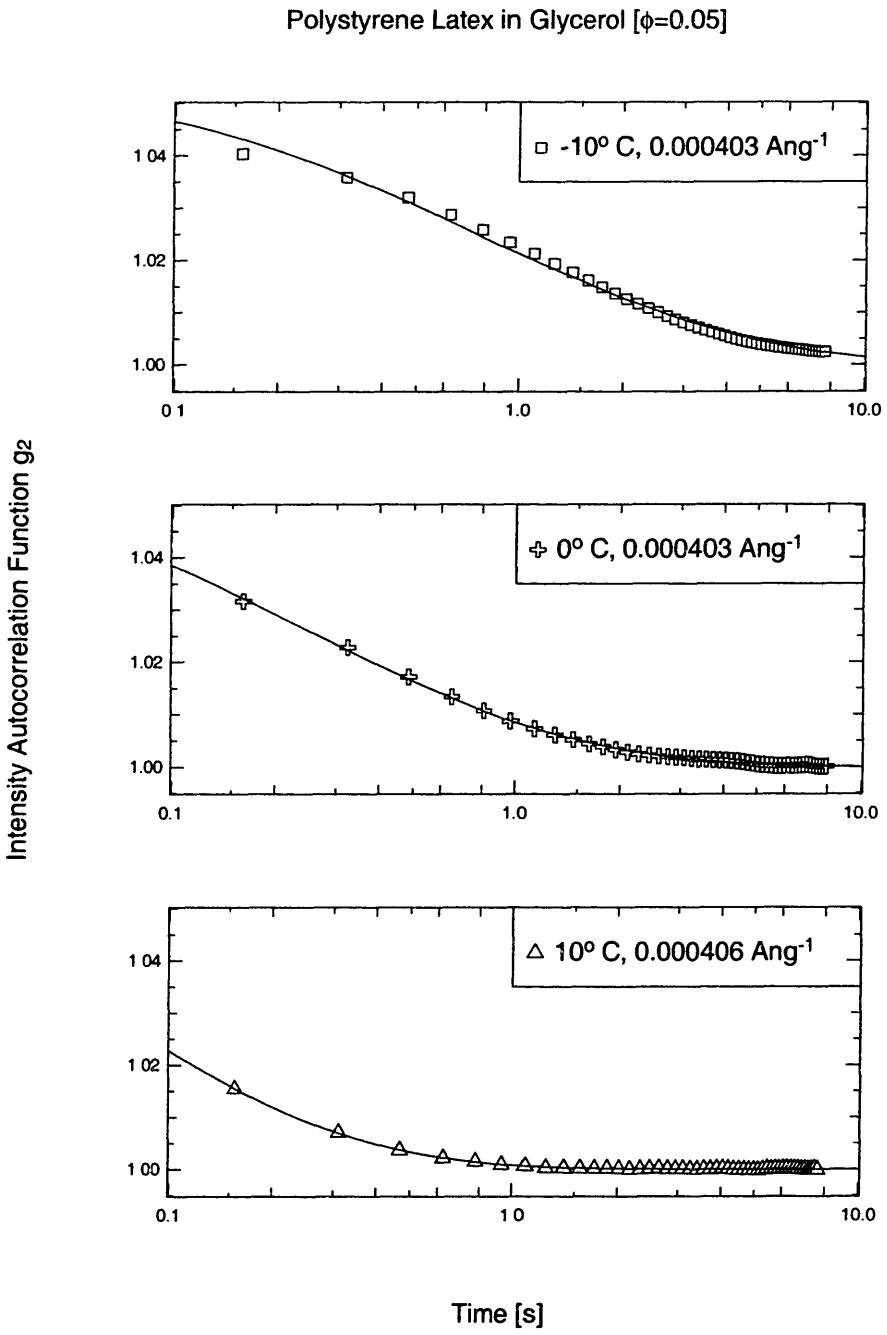

Figure 5-7: $g_2(t)$ for $\phi = 0.05$ at -10 C, 0 C, and 10 C at approximately similar values of q. The value of the speckle contrast for -10 C and 0 C is consistent with those in Figure 5-6, but the speckle contrast for 10 C cannot be accurately determined because of the inability to access times faster than approximately 0.1 seconds. As expected, the fitted baseline is essentially 1.

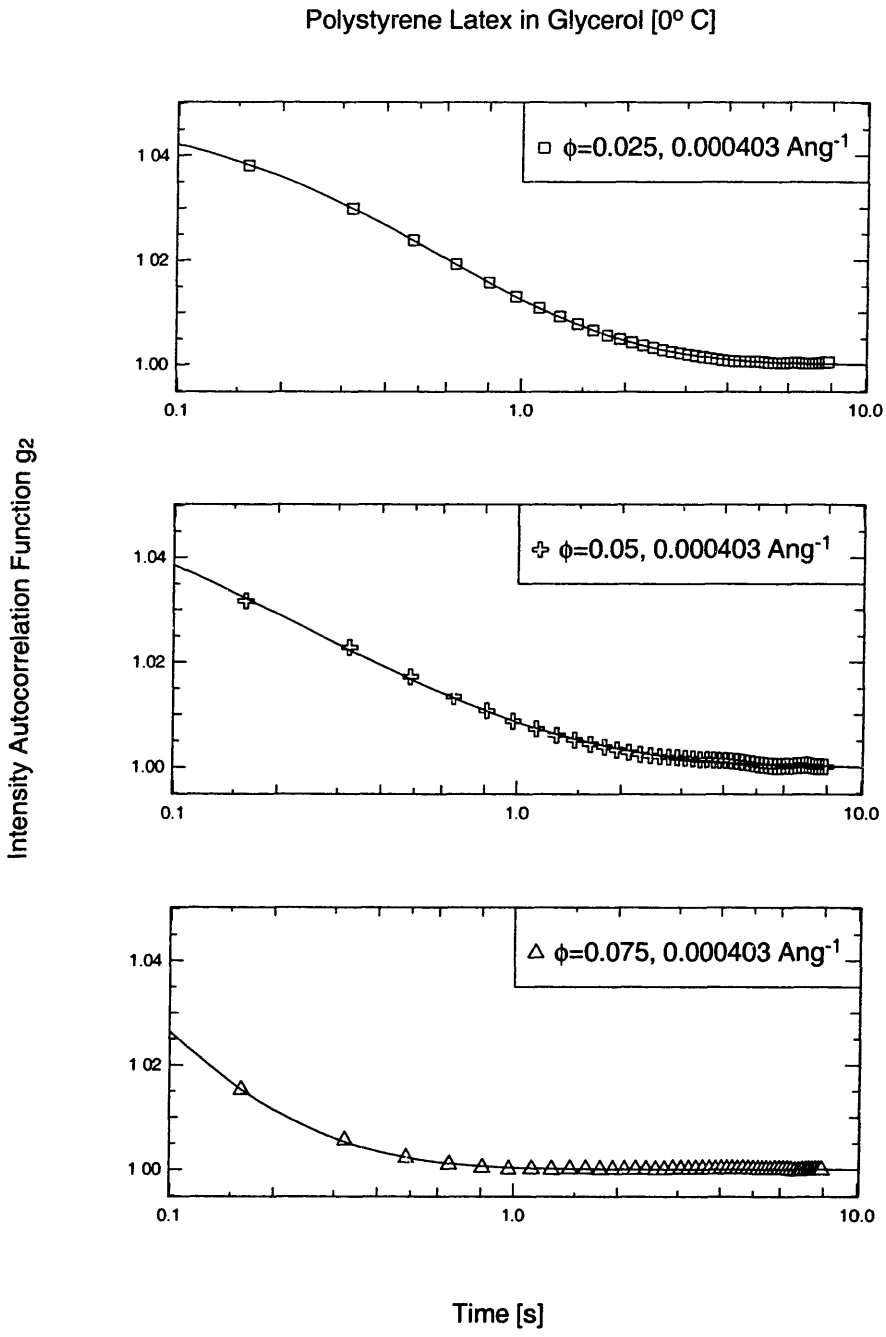

Figure 5-8: $g_2(t)$ for $\phi = 0.025, 0.05$, and 0.075 at 0 C at approximately similar values of q. The value of the speckle contrast for $\phi = 0.025$ and 0.05 is consistent with those in Figure 5-6, but the speckle contrast for $\phi = 0.075$ cannot be accurately determined because of the inability to access times faster than approximately 0.1 seconds. As expected, the fitted baseline is essentially 1.

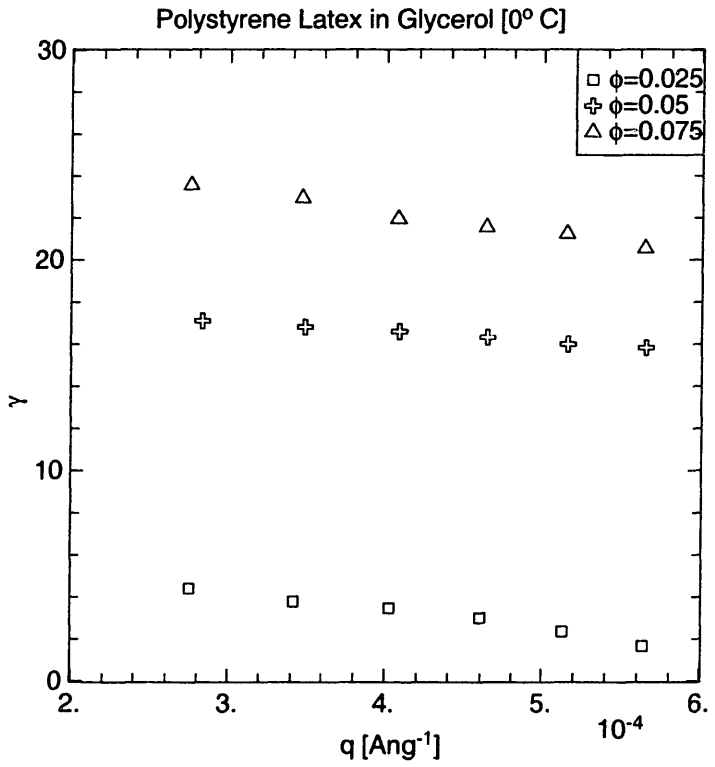

Figure 5-9: The fitted values of γ for $\phi = 0.025, 0.05,$ and 0.075 at 0 C for the 9 different values of q into which reciprocal space was partitioned during the fitting routine.

wavevectors ranging from 0.000156 Å^{-1} to 0.000376 Å^{-1} over three decades of time (0.1 seconds to 100 seconds). For the single scattering case we found that the intensity autocorrelation functions are dependent on the scattering angle, as predicted by theory. We also found that for our dilute samples, the time constants for the decay rate of the intensity autocorrelation functions are essentially constant across concentration. Our measurements in the multiple scattering regime spanned wavevectors ranging from 0.000158 Å^{-1} to 0.000714 Å^{-1} over two decades of time (0.1 seconds to 10 seconds). We found that $g_2(t)$ appears to be independent of the scattering angle, as predicted by theory. The data also appears to imply that the dynamics of our samples "speed up" with increasing temperature, another characteristic we expected to observe. We also found that for the range of volume fraction concentrations we probed, the intensity autocorrelation functions decay faster with increasing concentration.

Bibliography

[1] K. Schmitz. *Dynamic Light Scattering by Macromolecules.* Academic Press, Inc., New York, NY, 1990.

[2] F. Ferri. *Rev. Sci. Instrum.*, 68(6):1, 1997.

[3] H. Cummins and E. Pike, editors. *Photon Correlation and Light Beating Spectroscopy.* Plenum Press, New York, NY, 1973.

[4] D. Pine et. al. *Phys. Rev. Lett.*, 60:1134, 1988.

[5] W. Brown, editor. *Dynamic Light Scattering: The Method and Some Applications.* Oxford University Press, New York, NY, 1993.

[6] S. Fraden. *Phys. Rev. Lett.*, 65:512, 1990.

[7] H. Carslaw and J. Jaeger. *Conduction of Heat in Solids.* Clarendon Press, Oxford, 1990.

[8] D. Lumma. Unpublished. 1999.

[9] M. Van Albada and A. Lagendijk. *Phys. Rev. Lett.*, 55:2692, 1985.

[10] P. Wolf and G. Maret. *Phys. Rev. Lett.*, 55:2696, 1985.